JCI insight

RESEARCH ARTICLE

Accelerated osteocyte senescence and skeletal fragility in mice with type 2 diabetes

Brittany A. Eckhardt,[1,2] Jennifer L. Rowsey,[1,2] Brianne S. Thicke,[1,2] Daniel G. Fraser,[1,2] Katherine L. O'Grady,[3] Olga P. Bondar,[3] Jolaine M. Hines,[3] Ravinder J. Singh,[3] Andrew R. Thoreson,[4,5] Kuntol Rakshit,[6] Anthony B. Lagnado,[2,6] João F. Passos,[2,6] Adrian Vella,[1] Aleksey V. Matveyenko,[6] Sundeep Khosla,[1,2] David G. Monroe,[1,2] and Joshua N. Farr[1,2,6]

[1]Division of Endocrinology, [2]Robert and Arlene Kogod Center on Aging, [3]Immunochemical Core Laboratory, [4]Materials and Structural Testing Core, [5]Department of Physical Medicine and Rehabilitation, and [6]Division of Physiology and Biomedical Engineering, Mayo Clinic College of Medicine, Mayo Clinic, Rochester, Minnesota, USA.

The worldwide prevalence of type 2 diabetes (T2D) is increasing. Despite normal to higher bone density, patients with T2D paradoxically have elevated fracture risk resulting, in part, from poor bone quality. Advanced glycation endproducts (AGEs) and inflammation as a consequence of enhanced receptor for AGE (RAGE) signaling are hypothesized culprits, although the exact mechanisms underlying skeletal dysfunction in T2D are unclear. Lack of inducible models that permit environmental (in obesity) and temporal (after skeletal maturity) control of T2D onset has hampered progress. Here, we show in C57BL/6 mice that a onetime pharmacological intervention (streptozotocin, STZ) initiated in adulthood combined with high-fat diet–induced (HFD-induced) obesity caused hallmark features of human adult-onset T2D, including prolonged hyperglycemia, insulin resistance, and pancreatic β cell dysfunction, but not complete destruction. In addition, HFD/STZ (i.e., T2D) resulted in several changes in bone quality that closely mirror those observed in humans, including compromised bone microarchitecture, reduced biomechanical strength, impaired bone material properties, altered bone turnover, and elevated levels of the AGE CML in bone and blood. Furthermore, T2D led to the premature accumulation of senescent osteocytes with a unique proinflammatory signature. These findings highlight the RAGE pathway and senescent cells as potential targets to treat diabetic skeletal fragility.

Introduction

Type 2 diabetes (T2D) is a chronic progressive disease characterized by several pathogenic abnormalities that together contribute to dysfunctional insulin secretion and signaling caused by compromised pancreatic β cell function and insulin resistance in multiple tissues, resulting in increased blood glucose levels (hyperglycemia) (1, 2). Pancreatic β cells, along with their secretory product insulin, are central to normal energy homeostasis and to the pathophysiology of T2D. Under normal conditions β cells vary insulin secretion considerably so that high postprandial insulin concentrations stimulate glucose uptake in insulin-sensitive organs. Obesity is a common cause of insulin resistance in humans. However, most obese individuals are not diabetic because via β cell compensation they can increase their daily rates of insulin secretion 3- to 4-fold relative to lean controls to thereby maintain normal glucose levels (3). Notwithstanding, over time as β cells fail and cannot match insulin requirements, T2D develops.

During the initial onset and progression of T2D, insulin resistance is accompanied by compensatory increased β cell insulin release, although as the disease progresses, these compensatory adaptation mechanisms become insufficient to maintain blood glucose homeostasis, eventually leading to progressive functional and morphological β cell deterioration (4). As such, in humans with T2D more than 50% of β cell function has been compromised at the time of diagnosis (5). Therefore, the overt hyperglycemia in patients diagnosed with "frank" T2D is characterized by insulin resistance and insulin deficiency largely resulting from the loss of β cell function and/or mass.

Despite normal to higher bone mineral density (BMD) (6), humans with T2D paradoxically have increased fracture risk (7). Poor bone quality has been observed in human diabetic bone biopsies (8). Advanced glycation endproducts (AGEs) and inflammatory factors have been hypothesized as potential

Conflict of interest: The authors have declared that no conflict of interest exists.

Submitted: November 25, 2019
Accepted: March 26, 2020
Published: May 7, 2020.

Reference information: *JCI Insight*. 2020;5(9):e135236. https://doi.org/10.1172/jci.insight.135236.

mediators (9), although our knowledge of the pathophysiological mechanisms underlying skeletal dysfunction in T2D is incomplete. Lack of animal models that faithfully recapitulate the key metabolic and skeletal phenotypes of the human condition has hampered progress, underscoring the need to develop new models. Among the available species, the mouse has several advantages for this purpose. This will be an important step toward identifying and optimizing novel approaches to treat diabetic skeletal fragility. However, a major limitation of most T2D rodent models is that the onset of disease often occurs before skeletal maturity (10), which is problematic for studying the effects of adult-onset T2D on the skeleton.

We have previously identified senescent cells in the bone microenvironment with aging (11) and found that targeting cellular senescence improved age-related bone loss (12). Furthermore, senescence has been shown to increase in adipose tissue, liver, and brain during obesity (13–15) and in pancreatic β cells, contributing to T2D (16). This led us to hypothesize that cellular senescence may be a mechanistic link between poor bone quality and T2D.

In the current study, we investigated the roles of adult-onset T2D in mediating skeletal fragility and explored potential underlying mechanisms responsible for causing these alterations. To pursue these aims, we utilized a nongenetic mouse model mimicking human T2D, induced during adulthood in the setting of obesity, that displays overt hyperglycemia, dysfunctional insulin secretion, insulin resistance, and β cell deterioration — i.e., the high-fat diet (HFD)/streptozotocin (STZ) mouse of T2D (17–19). Here, we show that mice with adult-onset T2D have impaired bone quality, altered bone turnover, elevated levels of N^{ε}-(1-carboxymethyl)-L-lysine (CML) — an activator of the receptor for AGE (RAGE) pathway (20) — and accelerated cellular senescence (21).

Results

Body composition of the HFD/STZ mouse model of T2D. At study onset (i.e., before diet initiation), mice in all 4 groups (Figure 1A) were well matched for body weight. Following diet randomization and the 4-week lead-in phase of diet acclimation, both groups receiving HFD (HFD/VEH and HFD/STZ) had significantly higher body weights; as anticipated, obesity in these mice persisted throughout the 12-week experimental phase of the study (Figure 1B). Body weights did not differ between the LFD/VEH (control) and LFD/STZ mice at any time point (Figure 1B), whereas at study endpoint mice receiving HFD/VEH or HFD/STZ had body weights that were 30% ($P < 0.001$) and 18% ($P < 0.01$) higher, respectively, than control mice (Figure 1C). The increased body weights in the HFD-treated animals were predominantly due to gains in adiposity because both after the lead-in phase (i.e., at baseline; Figure 1D) and at endpoint (Figure 1E), fat mass in the HFD/VEH and HFD/STZ groups was, on average, significantly (all $P < 0.05$) higher than control mice. Lesser changes were observed in lean mass in response to HFD, particularly at baseline (Figure 1F), although by endpoint mice on HFD alone (HFD/VEH) tended to have more lean mass (Figure 1G). By contrast, STZ in the absence of HFD (i.e., LFD/STZ) had no overt effects on either fat or lean mass at any time point (Figure 1, D–G).

Metabolic dysfunction in the HFD/STZ mouse model of T2D. To generate a nongenetic animal model of human adult-onset T2D in the setting of obesity that displays overt hyperglycemia, dysfunctional insulin secretion, and β cell deterioration — i.e., the HFD/STZ mouse model of T2D, as done previously (17–19), mice randomized to the HFD/STZ group were acclimated to HFD for 4 weeks and then injected with a single, relatively low dose of STZ, followed by continuous HFD feeding for an additional 12 weeks (Figure 2A; Supplemental Figure 1A; supplemental material available online with this article; https://doi.org/10.1172/jci.insight.135236DS1). Importantly, neither HFD feeding alone (HFD/VEH) nor STZ treatment alone (LFD/STZ) was sufficient to cause diabetes or alter circulating glucose levels, which consistently remained less than 200 mg/dL and were essentially identical to those observed in control (LFD/VEH) mice; in contrast, the combination of HFD/STZ was necessary to cause persistent, overt hyperglycemia (Figure 2B; Supplemental Figure 1, B–D), defined in mice as glucose levels higher than 250 mg/dL (10, 22). Indeed, between weeks 2 and 12 after STZ injection in the setting of HFD, median circulating glucose levels of HFD/STZ mice ranged between 70% and 88% higher (all $P < 0.001$) relative to each of the other 3 groups (Figure 2C). Consistent with this, HFD/STZ mice had circulating hemoglobin A1c (HbA1c) levels that were 44% to 60% higher at midpoint (week 6; all $P < 0.001$) and 43% to 57% higher at endpoint (week 12; all $P < 0.001$) of the experimental phase (Figure 2D; Supplemental Figure 1, E–G). Because of pancreatic β cell compensation, mice on HFD alone (HFD/VEH) were able to increase their plasma insulin levels, on average, by greater than 2-fold at both midpoint ($P < 0.001$) and endpoint ($P < 0.001$) as compared with control (LFD/VEH) mice (Figure 2D; Supplemental Figure 1, H–J). By contrast, the

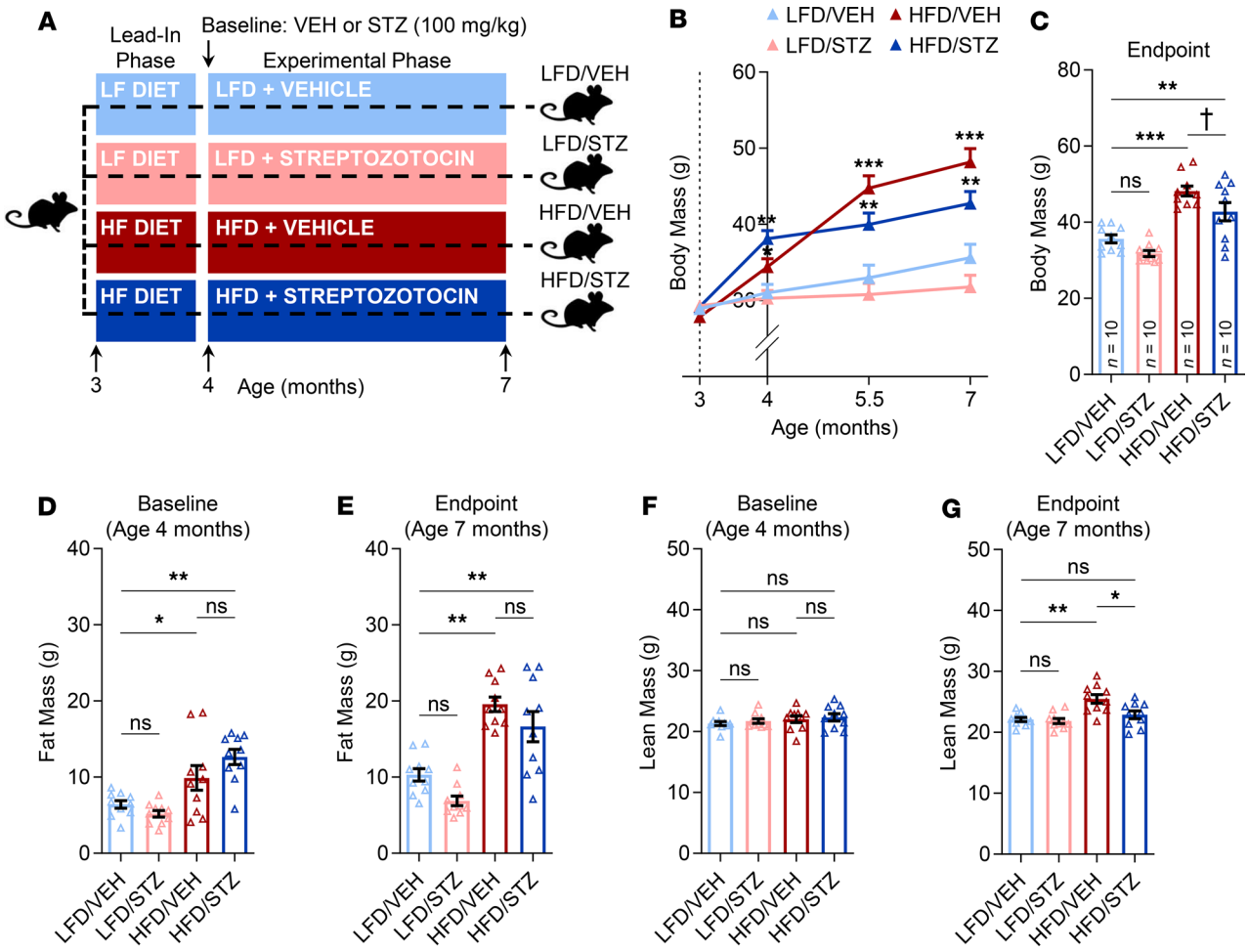

Figure 1. Body composition of the HFD/STZ mouse model of T2D. (**A**) Schematic of the study design depicting male C57BL/6 mice (n = 10/group) randomized to either LFD (10% kcal from fat) or HFD (60% kcal from fat) for 1 month (lead-in phase) followed by treatment (at baseline) with either VEH or STZ and follow-up for 3 months (experimental phase) out to 7 months of age (endpoint): LFD/VEH, LFD/STZ, HFD/VEH, HFD/STZ (n = 10/group). (**B**) Compared with control mice fed LFD (LFD/VEH group), mice fed an HFD (and subsequently treated with either VEH or STZ) exhibited significant gains in body weight over the course of 4 months. (**C**) Body weight comparisons among the 4 groups at endpoint (age 7 months). (**D**) Comparisons of fat mass at baseline after 1 month of diet (lead-in phase). (**E**) Fat mass comparisons among the 4 groups at endpoint (age 7 months). (**F**) Comparisons of lean mass at baseline after 1 month of diet (lead-in phase). (**G**) Lean mass comparisons among the 4 groups at endpoint (age 7 months). For all analyses, n = 10/group. Data represent mean ± SEM (error bars). ns, $P \geq 0.10$; $^{\dagger}P < 0.10$; $^{*}P < 0.05$; $^{**}P < 0.01$; $^{***}P < 0.001$ (1-way ANOVA with post hoc Tukey's correction for multiple comparisons). HFD, high-fat diet; STZ, streptozotocin; T2D, type 2 diabetes; LFD, low-fat diet; VEH, vehicle.

relatively low dose of STZ caused modest reductions in plasma insulin levels in LFD/STZ and HFD/STZ mice (Figure 2E; Supplemental Figure 1, H–J). These levels of insulin were consistent with those reported in previous studies (17–19); however, it is important to note that in the absence of obesity (LFD/STZ), the modest hypoinsulinemia was not sufficient to cause hyperglycemia, whereas in contrast this same level of reduced insulin caused hyperglycemia in the setting of insulin resistance induced by HFD in mice receiving STZ (Figure 2B; Supplemental Figure 1 B–D; Figure 2E; Supplemental Figure 1, H–J). Finally, these data were confirmed by morphometric analysis of pancreatic β cell islet morphology and composition. In agreement with β cell compensation and the increased plasma insulin levels observed in mice on HFD alone (HFD/VEH), examination of pancreatic islets revealed large insulin-positive β cell cores (Figure 2F), and (via analysis of whole pancreata sections) these animals were found to have a 63% higher β cell area ($P <$ 0.001) as compared with control (LFD/VEH) mice (Figure 2, F and G). By contrast, mice receiving HFD feeding and low-dose STZ injection (HFD/STZ) had a fairly dramatic reduction (by –86%) in pancreatic β cell area as compared with control mice (Figure 2, F and G). Thus, because adult HFD/STZ mice manifest hyperglycemia, impaired insulin secretion, insulin resistance, and pancreatic β cell deterioration, hallmark features of T2D, we chose this model to examine the consequences of adult-onset T2D on the skeleton.

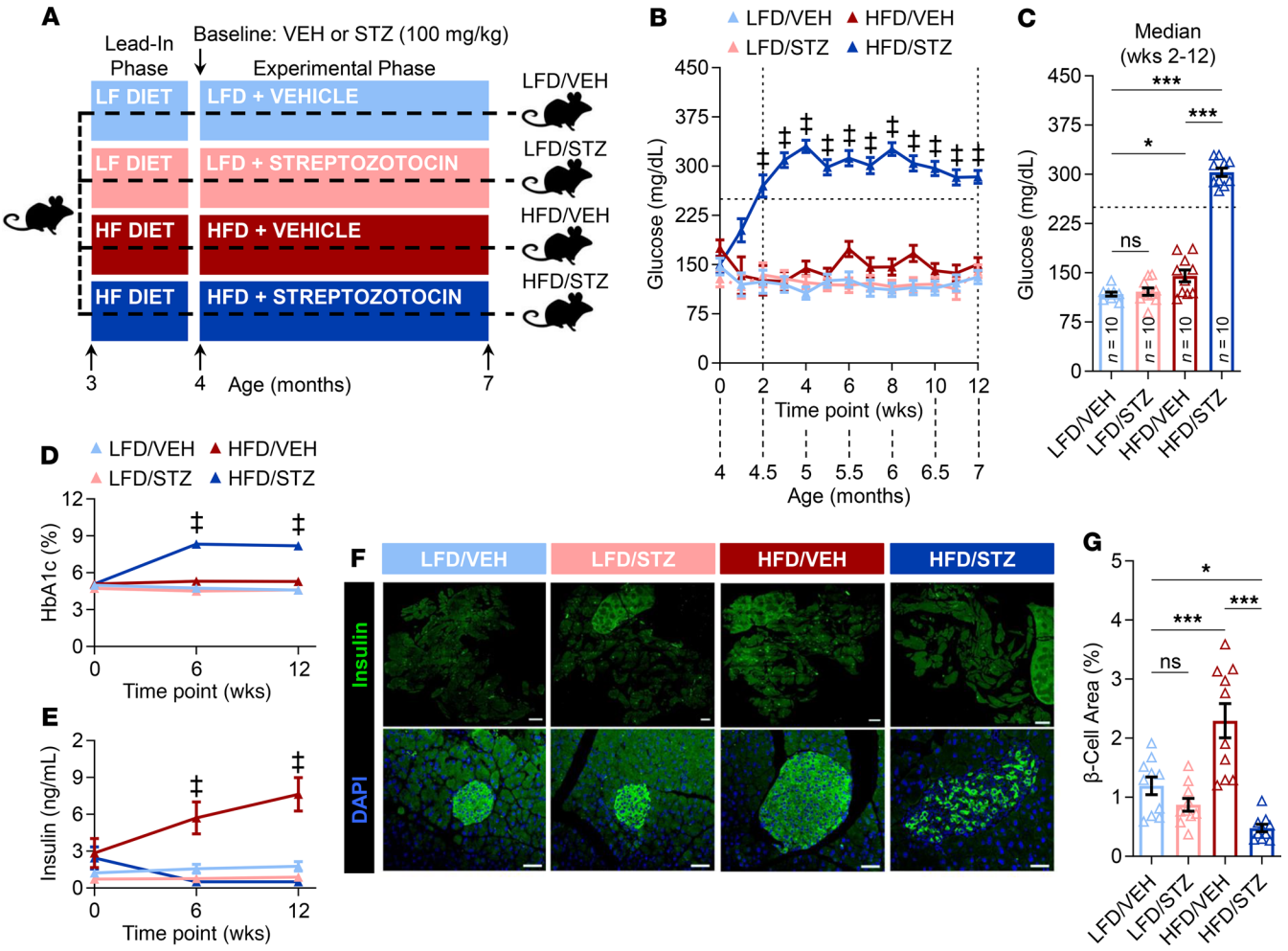

Figure 2. Effects of HFD/STZ on metabolic and pancreatic β cell parameters. (**A**) Schematic of the study design depicting male C57BL/6 mice (n = 10/group) randomized to either LFD (10% kcal from fat) or HFD (60% kcal from fat) for 1 month (lead-in phase) followed by treatment (at baseline) with either VEH or STZ and follow-up for 3 months (experimental phase) out to 7 months of age (endpoint): LFD/VEH, LFD/STZ, HFD/VEH, HFD/STZ (n = 10/group). (**B**) Compared with each of the 3 other groups, HFD/STZ mice exhibited significantly higher nonfasted glucose levels (taken weekly from tail blood) 2 weeks after receiving STZ that were maintained throughout the remainder of the study. (**C**) Comparisons of median glucose concentrations (weeks 2–12) among the 4 groups. (**D**) Compared with each of the 3 other groups, HFD/STZ mice exhibited significantly higher nonfasted HbA1c levels (taken from tail blood) at midpoint and endpoint of the experimental phase. (**E**) Mice fed HFD alone (HFD/VEH) can significantly increase their circulating insulin concentrations, whereas HFD/STZ mice cannot activate this compensatory mechanism in order to maintain their blood glucose levels in the physiological range due to functional β cell deterioration. (**F**) Immunohistochemical analyses of pancreatic β cells with the overlay of insulin (shown in green) and DAPI-positive nuclei (shown in blue) demonstrate that mice fed HFD alone (HFD/VEH) exhibit significantly greater β cell masses and insulin-positive areas, whereas HFD/STZ mice exhibit loss of β cell function and mass, consistent with a model of T2D. (**G**) Quantification of comparisons of β cell area among the 4 groups. For all analyses, n = 10/group. Data represent mean ± SEM (error bars). ns, $P \geq 0.10$; $^{*}P < 0.05$; $^{***}P < 0.001$ (1-way ANOVA with post hoc Tukey's correction for multiple comparisons); $^{‡}P < 0.001$ versus each of the 3 other groups (1-way ANOVA with post hoc Tukey's correction for multiple comparisons). HFD, high-fat diet; STZ, streptozotocin; T2D, type 2 diabetes; LFD, low-fat diet; VEH, vehicle.

Skeletal phenotype of the HFD/STZ mouse model of T2D. To begin to examine the skeletal phenotype of the animals, we initially used micro–computed tomography (μCT). This included ex vivo μCT scanning at study endpoint (age 7 months) of the lumbar spine and proximal tibia metaphysis. In addition, because of the potential confounding effects of HFD on skeletal parameters during the lead-in phase of diet acclimation, we also performed in vivo μCT scanning at baseline (age 4 months) and endpoint (age 7 months) of the experimental phase (Figure 3A; Supplemental Figure 2A) at both the proximal metaphysis (trabecular site) and diaphysis (cortical site) of the tibia. First, to test for any potential effects of STZ alone on the skeleton, we compared bone parameters of LFD/STZ mice with those of control (LFD/VEH) mice. As shown in Supplemental Figure 2, B–N, the low-dose STZ injection by itself, in the setting of LFD feeding, had no significant effects on any bone parameters at either the spine or tibia. We next examined the effects

of obesity alone (HFD/VEH) versus T2D (HFD/STZ) on μCT-derived bone parameters as compared with control (LFD/VEH) mice. At study endpoint, cross-sectional ex vivo μCT analysis did not detect significant ($P > 0.05$) effects of either obesity alone or T2D on trabecular bone volume fraction (BV/TV) at the lumbar spine (Figure 3B) or tibia metaphysis (Figure 3C). Longitudinal in vivo μCT analysis at the tibia metaphysis revealed that, on average, each of the groups of mice lost trabecular bone; however, whereas obesity alone had a modest, albeit nonsignificant ($P > 0.05$), detrimental effect on trabecular BV/TV, T2D caused significantly ($P < 0.05$) more trabecular bone loss over time as compared with that observed in control mice (Figure 3D). Furthermore, as compared with changes observed in control mice, T2D had detrimental effects over time on cortical bone parameters at the tibia metaphysis, including a trend for reduced cortical volumetric BMD (vBMD) (Figure 3E; $P = 0.09$) and significant cortical thinning (Figure 3F; $P < 0.05$) due to reduced outer bone size because although endocortical circumference did not change (Figure 3G; $P > 0.05$), periosteal circumference was significantly reduced (Figure 3H; $P < 0.05$), ultimately leading to significantly ($P < 0.05$) diminished bone strength (i.e., failure load) as assessed by micro–finite element analysis (μFEA) (Figure 3I). In addition, similar changes were observed in the T2D as compared with control mice at the tibia diaphysis, including significantly reduced cortical vBMD (Figure 3J; $P < 0.05$), although the significantly thinner cortex (Figure 3K; $P < 0.05$) at this site was due to greater loss of bone on the inner surface because significant endocortical expansion was observed (Figure 3L; $P < 0.05$) with no change in periosteal circumference (Figure 3M; $P > 0.05$). Consistent with reductions in bone strength at the metaphysis, failure load at the tibia diaphysis was significantly reduced in T2D as compared with control mice (Figure 3N). In contrast, relative to control mice obesity alone (HFD/VEH) had nonsignificant (all $P > 0.05$) effects over time on cortical bone parameters and failure load at both the tibia metaphysis and diaphysis (Figure 3, E–N).

Bone quality properties of the HFD/STZ mouse model of T2D. To more rigorously examine the skeletal phenotype of the mice, we next examined several aspects of bone quality, including directly measured bone strength (i.e., compression loading at the spine and 3-point bending at the femur) as well as assessments of bone material properties (i.e., nanoindentation at the spine and reference point microindentation [RPI] at the femur). Because these tests can be performed ex vivo only, they were all done at study endpoint (Figure 4A; Supplemental Figure 3A). Consistent with findings observed by μCT, the low-dose STZ injection by itself, in LFD/STZ mice, had no significant (all $P > 0.05$) effects on bone quality parameters at either the spine or tibia as compared with control mice (Supplemental Figure 3, B–K). Similarly, bone quality parameters did not differ significantly (all $P > 0.05$) between obese alone (HFD/VEH) and control mice (Figure 4, B–K). By contrast, as compared with the latter group, despite the relatively short duration of the experimental phase (12 weeks), T2D in HFD/STZ mice altered multiple aspects, but not all parameters, reflecting bone quality. For example, whereas stiffness (Figure 4B; $P > 0.05$) and ultimate load (Figure 4C; $P > 0.05$) did not differ between groups, spine ultimate stress was significantly lower (by –24%; $P < 0.05$) in T2D relative to control mice (Figure 4D). Furthermore, femur stiffness was significantly lower (by –14%; $P < 0.05$) in T2D as compared with control mice (Figure 4E), although ultimate load (Figure 4F; $P > 0.05$) and failure energy (Figure 4G; $P > 0.05$) did not differ between T2D and control mice. With regard to material properties, nanoindentation testing of trabecular bone at the spine did not detect significant differences between T2D and control mice in either modulus (Figure 4H; $P > 0.05$) or hardness (Figure 4I; $P > 0.05$). However, as compared with control mice, RPI testing at the femur revealed that mice with T2D had, on average, significantly higher (by 13%; $P < 0.05$) total indentation distance increase (TID) values (Figure 4J) and significantly lower (by –19%; $P < 0.05$) average loading slope values (Figure 4K) — i.e., indications that the bone material of T2D mice at the tissue level exhibited lower fracture toughness and impaired ability to resist microcrack propagation, respectively.

Given that bone microarchitecture and bone quality properties were not significantly affected by either STZ alone (LFD/STZ) or obesity alone (HFD/VEH), we focused the subsequent, more in-depth analyses on the T2D (HFD/STZ) and control (LFD/VEH) groups (Figure 5A).

Bone histomorphometry and bone turnover markers in the HFD/STZ mouse model of T2D. Endocortical bone histomorphometry demonstrated significantly higher bone resorption (i.e., osteoclast numbers per bone perimeter, N.Oc/B.Pm, by 58%; $P < 0.05$) in T2D as compared with control mice (Figure 5B), without a coupled change in osteoblasts (i.e., N.Ob/B.Pm; Figure 5C; $P > 0.05$). However, bone formation indices were significantly reduced in T2D relative to control mice, including mineral apposition rate (MAR; Figure 5D, by –34%; $P < 0.05$) and bone formation rate per bone surface (BFR/BS; Figure 5E, by –52%; $P < 0.05$). Consistent with these changes at the cellular level, circulating levels of the bone resorption marker, cross-linked

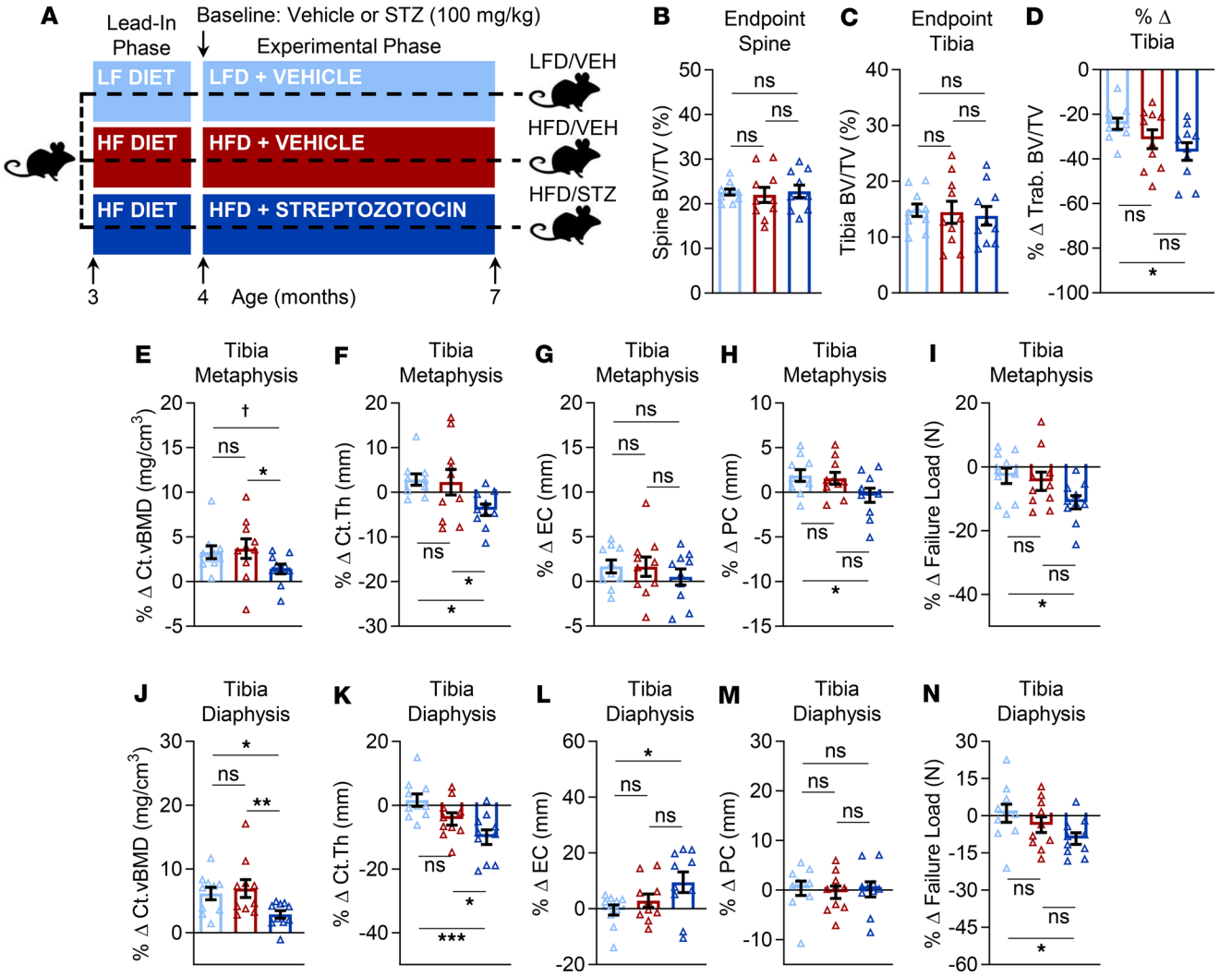

Figure 3. Short-term T2D, but not HFD alone, causes deterioration of bone microarchitecture. (**A**) Schematic of the study design depicting male C57BL/6 mice randomized to either LFD (10% kcal from fat) or HFD (60% kcal from fat) for 1 month (lead-in phase) followed by treatment (at baseline) with either VEH or STZ and follow-up for 3 months (experimental phase) out to 7 months of age (endpoint): LFD/VEH, HFD/VEH, HFD/STZ (n = 10/group). (**B**–**C**) Quantification of μCT-derived BV/TV (%) assessed ex vivo at the lumbar spine and tibia metaphysis at study endpoint. (**D**) Percentage change (% Δ) in trabecular BV/TV at the tibia metaphysis assessed by longitudinal in vivo μCT analysis (at baseline and endpoint). Longitudinal percentage changes in (**E**) cortical volumetric bone mineral density (Ct.vBMD, mg/cm^3), (**F**) cortical thickness (Ct.Th, mm), (**G**) endocortical circumference (EC, mm), (**H**) periosteal circumference (PC, mm), and (**I**) μFEA-derived failure load (N, Newton, an index of bone strength) at the tibia metaphysis. Longitudinal percentage changes in (**J**) Ct.vBMD (mg/cm^3), (**K**) Ct.Th (mm), (**L**) EC (mm), (**M**) PC (mm), and (**N**) μFEA-derived failure load (N) at the tibia diaphysis. For all analyses, n = 10/group. Data represent mean ± SEM (error bars). ns, $P \geq 0.10$; $^{\dagger}P < 0.10$; $^{*}P < 0.05$; $^{**}P < 0.01$; $^{***}P < 0.001$ (1-way ANOVA with post hoc Tukey's correction for multiple comparisons). HFD, high-fat diet; STZ, streptozotocin; T2D, type 2 diabetes; LFD, low-fat diet; VEH, vehicle.

C-telopeptide of type I collagen (CTx), were significantly higher (by 38%; $P < 0.05$) in T2D as compared with control mice (Figure 5F), whereas no difference was observed between groups in circulating levels of the bone formation marker, amino-terminal propeptide of type I collagen (P1NP) (Figure 5G; $P > 0.05$).

Expression of osteoblast lineage markers and factors that control bone remodeling in the HFD/STZ mouse model of T2D. We next used real-time quantitative polymerase chain reaction (rt-qPCR) to investigate the effects of T2D on the expression of osteoblast and osteocyte lineage markers as well as factors that control bone remodeling (i.e., *Tnfrsf11b*, OPG; and *Tnfsf11*, RANKL) in bone samples that were depleted of marrow elements (as described in Methods). Relative to controls, mice with T2D had significantly lower mRNA expression levels of the osteoblast lineage markers, *Runx2* and *Sp7* (osterix) (Figure 5H), whereas no significant differences were observed between the groups in expression of osteocyte lineage markers (Figure 5I). Furthermore, the mRNA expression of osteoprotegerin (*Opg*),

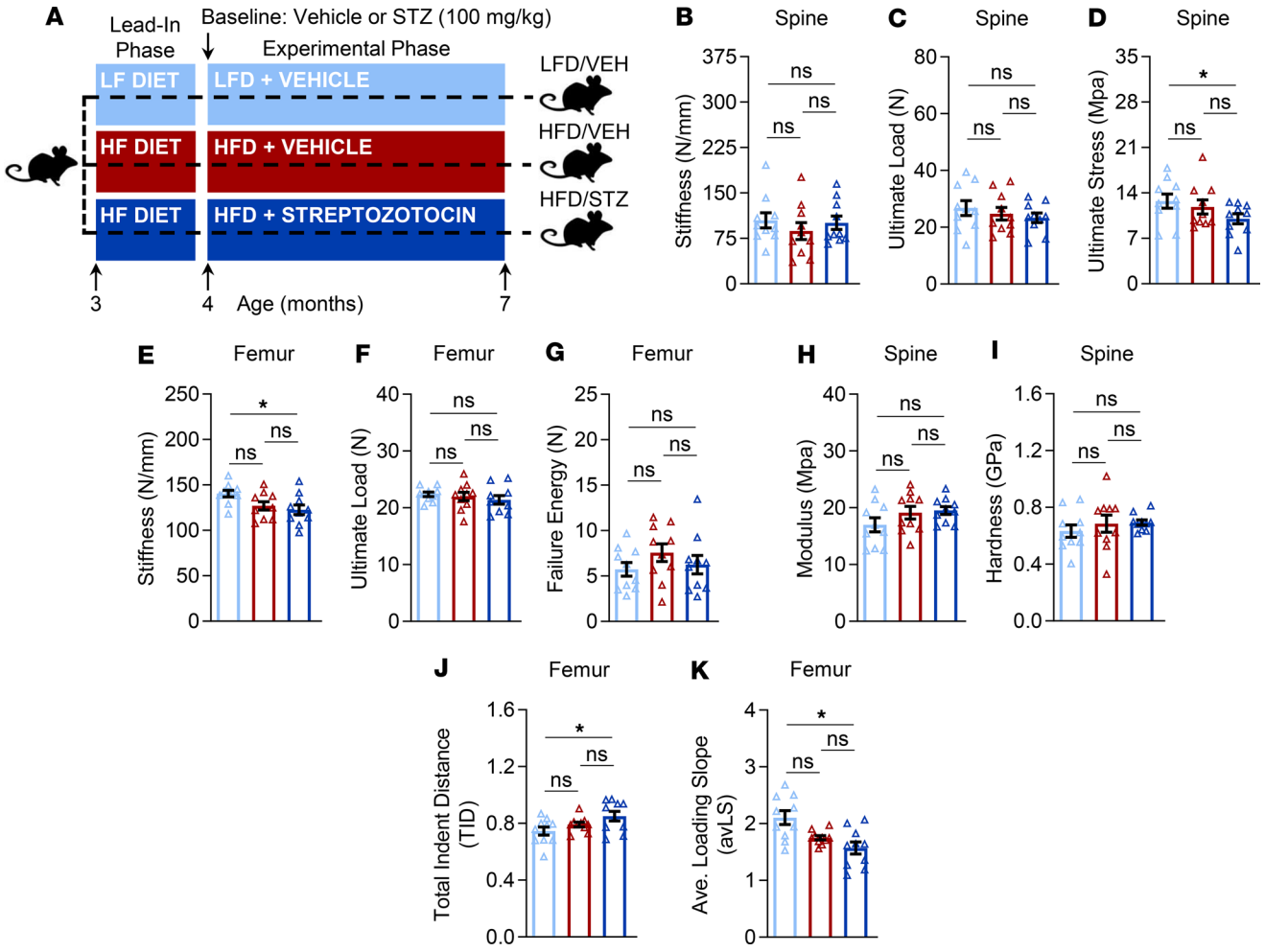

Figure 4. Short-term T2D has modest deleterious effects on bone biomechanical strength and material properties. (**A**) Schematic of the study design depicting male C57BL/6 mice randomized to either LFD (10% kcal from fat) or HFD (60% kcal from fat) for 1 month (lead-in phase) followed by treatment (at baseline) with either VEH or STZ and follow-up for 3 months (experimental phase) out to 7 months of age (endpoint): LFD/VEH, HFD/VEH, HFD/STZ (n = 10/group). Comparisons among the groups at study endpoint (7 months of age) of bone biomechanical properties (assessed by compression testing) at the lumbar vertebrae, including (**B**) stiffness (N/mm), (**C**) ultimate load (N), and (**D**) ultimate stress (MPa). Endpoint comparisons of bone biomechanical properties (assessed by 3-point bending) at the femur midshaft, including (**E**) stiffness (N/mm), (**F**) ultimate load (N), and (**G**) failure energy (N). Endpoint comparisons of bone material properties (assessed by nanoindentation) at the lumbar vertebrae, including (**H**) modulus (GPa) and (**I**) hardness (GPa). Endpoint comparisons of indices of bone material properties (assessed by reference point microindentation [RPI]) at the femur diaphysis, including (**J**) total indentation distance (TID) and (**K**) average loading slope (avLS). For all analyses, n = 10/group. Data represent mean ± SEM (error bars). ns, $P \geq 0.10$; *$P < 0.05$ (1-way ANOVA with post hoc Tukey's correction for multiple comparisons). HFD, high-fat diet; STZ, streptozotocin; T2D, type 2 diabetes; LFD, low-fat diet; VEH, vehicle.

an antagonist of receptor activator of NF-κB ligand (RANKL), did not differ between the groups (Figure 5J); however, consistent with the increased bone resorption levels (detected both at the cellular level and in circulation), the mRNA expression of *Rankl*, which is required for osteoclast formation and survival, was significantly higher in bone samples of T2D relative to control mice (Figure 5K).

Bone and circulating AGEs in the HFD/STZ mouse model of T2D. AGEs are a category of posttranslational modification reactions (typically between sugars and proteins) that are associated with the degradation or alteration of tissue properties in the settings of, for example, aging and diabetes (23, 24). To determine whether AGEs accumulate to a greater extent in biological samples, including bone tissue and serum, of T2D versus control mice (Figure 6A), we developed liquid chromatography–tandem mass spectrometry (LC-MS/MS) assays to accurately quantify 2 commonly measured AGEs — CML and pentosidine (as described in Methods). This approach revealed that levels of CML, a noncrosslink/nonfluorescent AGE (25), were significantly higher (by 31%; $P < 0.01$) in bone tissue samples of T2D as compared with control mice (Figure 6B). Consistent with this finding, serum levels of CML were also significantly higher (by 45%; $P < 0.05$) in

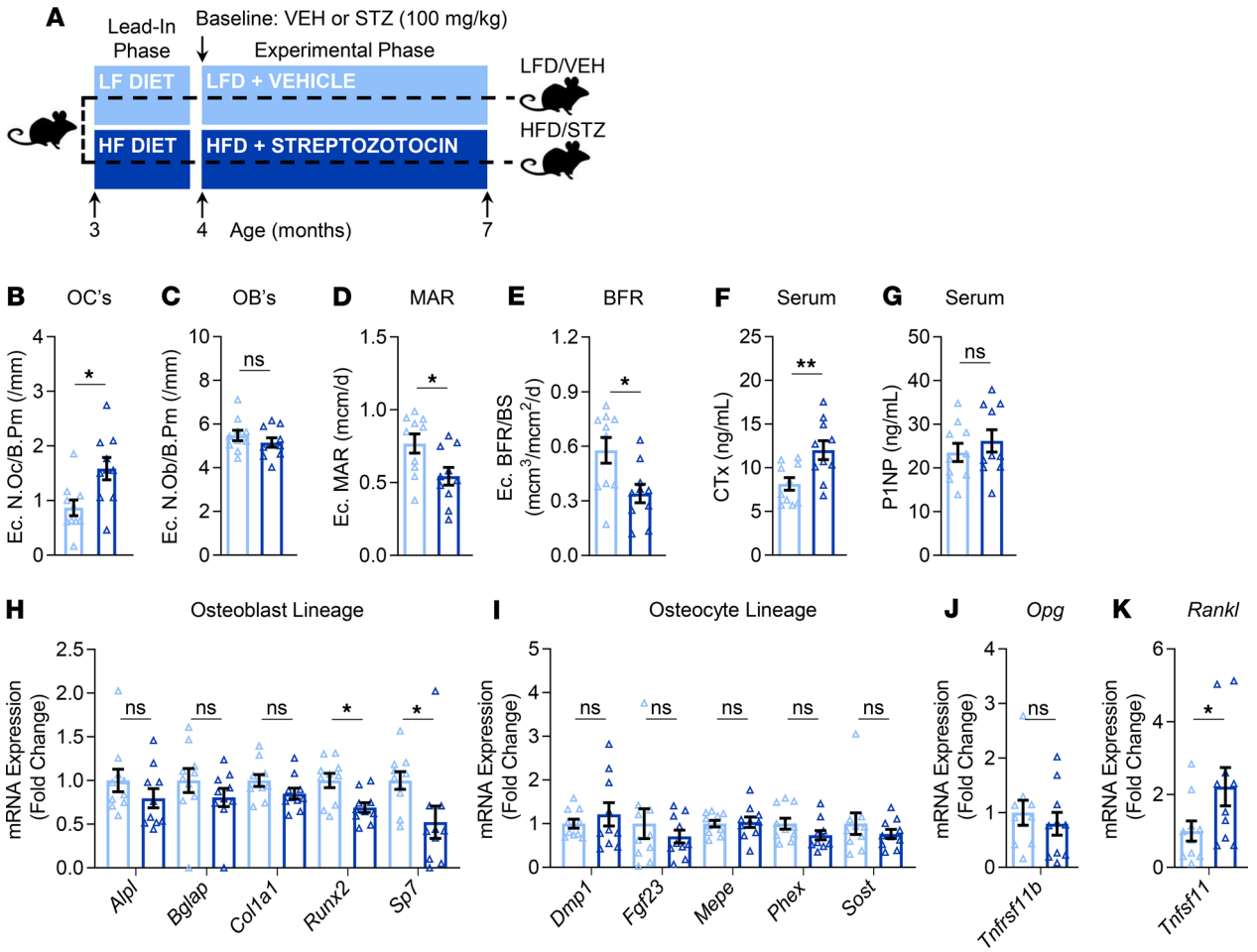

Figure 5. Effects of T2D on skeletal histomorphometry parameters, bone turnover markers, and bone gene expression markers. (**A**) Schematic of the study design depicting male C57BL/6 mice randomized to either LFD (10% kcal from fat) or HFD (60% kcal from fat) for 1 month (lead-in phase) followed by treatment (at baseline) with either VEH or STZ and follow-up for 3 months (experimental phase) out to 7 months of age (endpoint): LFD/VEH, HFD/STZ (n = 10/group). Histomorphometric quantification at the tibia endocortical (Ec.) surface of (**B**) osteoclast numbers per bone perimeter (N.Oc/B.Pm; /mm), (**C**) osteoblast numbers per bone perimeter (N.Ob/B.Pm; /mm), (**D**) mineral apposition rate (MAR; mcm/d), and (**E**) bone formation rate per bone surface (BFR/BS; mcm³/mcm²/d). Quantification of circulating serum bone turnover makers, including (**F**) the bone resorption marker, cross-linked C-telopeptide of type I collagen (CTx; ng/mL), and (**G**) the bone formation marker, amino-terminal propeptide of type I collagen (P1NP; ng/mL). rt-qPCR mRNA gene expression analyses of (**H**) osteoblast marker genes, (**I**) osteocyte genes, (**J**) osteoprotegerin (*Tnfrsf11b*, *Opg*), and (**K**) tumor necrosis factor ligand superfamily member 11 (*Tnfsf11*, *Rankl*) in bone samples. Data represent mean ± SEM (error bars). ns, $P \geq 0.10$; *$P < 0.05$; **$P < 0.01$ (independent samples t test or Wilcoxon's rank-sum test, as appropriate). HFD, high-fat diet; STZ, streptozotocin; T2D, type 2 diabetes; LFD, low-fat diet; VEH, vehicle; Ec, endocortical.

T2D relative to control mice (Figure 6C). By contrast, bone tissue levels of pentosidine, a fluorescent AGE crosslink formed between lysine and arginine (26), did not differ between the groups (Figure 6D; $P > 0.05$). It should be noted, however, that, perhaps surprisingly, levels of pentosidine in bone tissue were quite low and essentially undetectable (even by LC-MS/MS) in most serum samples (data not shown). As anticipated, levels of CML were found to be even higher in bone tissue (Supplemental Figure 4A) and serum (Supplemental Figure 4B) samples from old (24-month) wild-type (WT) mice as compared with T2D or young adult mice. Consistent with this finding, bone tissue levels of pentosidine also increased with aging (Supplemental Figure 4C), which provides further validation of our LC-MS/MS method.

Identification of senescent osteocytes and the senescence-associated secretory phenotype in the HFD/STZ mouse model of T2D. Cellular senescence is a stress response cell fate that entails proliferative arrest, profound chromatin changes, and typically acquisition of a proinflammatory secretome, termed the senescence-associated secretory phenotype (SASP) (21). In recent studies, our group has systematically identified an accumulation of senescent cells in the bone microenvironment with aging (11) and demonstrated a causal role for senescent cells in mediating age-related bone loss (12). In the current study, we compared cellular senescence biomarkers and the SASP between T2D and control mice. With T2D, we

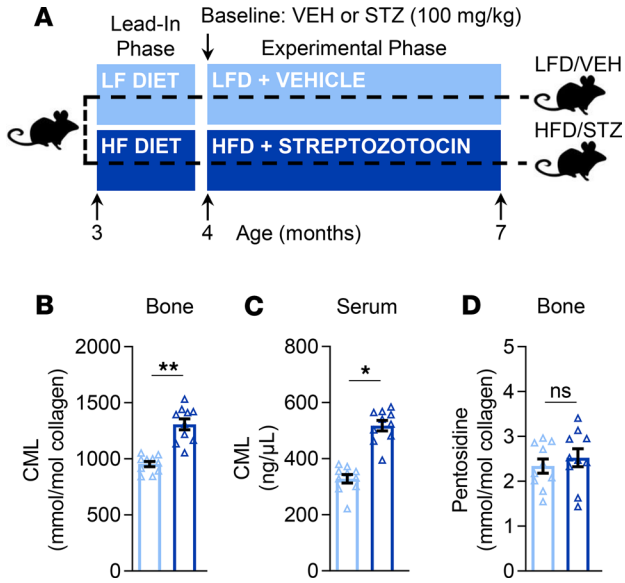

Figure 6. Effects of T2D on AGEs. (**A**) Schematic of the study design depicting male C57BL/6 mice randomized to either LFD (10% kcal from fat) or HFD (60% kcal from fat) for 1 month (lead-in phase) followed by treatment (at baseline) with either VEH or STZ and follow-up for 3 months (experimental phase) out to 7 months of age (endpoint): LFD/VEH, HFD/STZ (n = 10/group). CML levels in (**B**) bone tissue (mmol/mol collagen) and (**C**) serum (ng/μL) samples. (**D**) Pentosidine levels in bone tissue samples (mmol/mol collagen); note that pentosidine levels were detected at low to nondetectable levels in serum (data not shown). Data represent mean ± SEM (error bars). ns, $P \geq 0.10$; *$P < 0.05$; **$P < 0.01$ (independent samples t test). HFD, high-fat diet; STZ, streptozotocin; T2D, type 2 diabetes; LFD, low-fat diet; VEH, vehicle.

found in osteocyte-enriched bone samples by rt-qPCR that mRNA expression of the key mediator of cellular senescence, $p16^{Ink4a}$ (encoded by the Ink4a/Arf locus, also known as *Cdkn2a*) (21), was significantly elevated (by 64%; $P < 0.001$) as compared with control mice (Figure 7A). Expression of *Cdkn1a* ($p21^{Cip1}$), which can drive senescence in a context-specific manner (21), was also significantly elevated (by 47%; $P < 0.01$) in bone samples of T2D relative to control mice (Figure 7B). To further validate the greater accumulation of senescent cells in bone of T2D versus control mice, we used an established assay for cellular senescence, i.e., the senescence-associated distension of satellites (SADS) assay (27). As shown in Figure 7, C and D, the percentage of senescent osteocytes, defined as at least 4 SADS (characterized by large unraveling of pericentromeric DNA) per osteocyte, was significantly higher (nearly 2-fold; $P <$ 0.01) in bone cortices of T2D as compared with control mice. We next measured telomere-associated foci (TAF) (Figure 7E) — i.e., sites of DNA damage (γ-H2AX) colocalized with telomeres (28) — in osteocytes because TAF are a robust marker of cellular senescence. Significantly more TAF per osteocyte were found in cortical bone of T2D as compared with control mice (Figure 7F). Consistent with this, the percentage of TAF^+ osteocytes (defined as ≥1, ≥2, or ≥3 TAF per nuclei) was also significantly higher in bone cortices of T2D versus control mice (Figure 7G). Finally, we used rt-qPCR to measure the mRNA expression of a panel of 36 established SASP genes (29) in the osteocyte-enriched bone samples of T2D versus control mice (Figure 8, A and B). Interestingly, this analysis revealed a unique proinflammatory SASP composed predominantly of significantly (all $P < 0.05$) upregulated levels of matrix metalloproteinases (MMPs; i.e., *Mmp3*, *Mmp9*, *Mmp12*, and *Mmp13*). In addition, the expression of *Nfkb1* (NF-κB), a downstream target of the RAGE signaling pathway activated by CML (20), was also significantly ($P < 0.05$) elevated in the osteocyte-enriched bone samples of T2D as compared with control mice. Interestingly, in our previous study (11), we observed that significantly (all $P < 0.05$) upregulated levels of several SASP factors (23 of 36 analyzed) in osteocyte-enriched bone samples from old (24-month) relative to young adult (6-month) mice were not changed with T2D (Figure 8B), although elevated MMPs and NF-κB are features of the SASP signature of senescent osteocytes shared by both aging and T2D (Supplemental Figures 5 and 6).

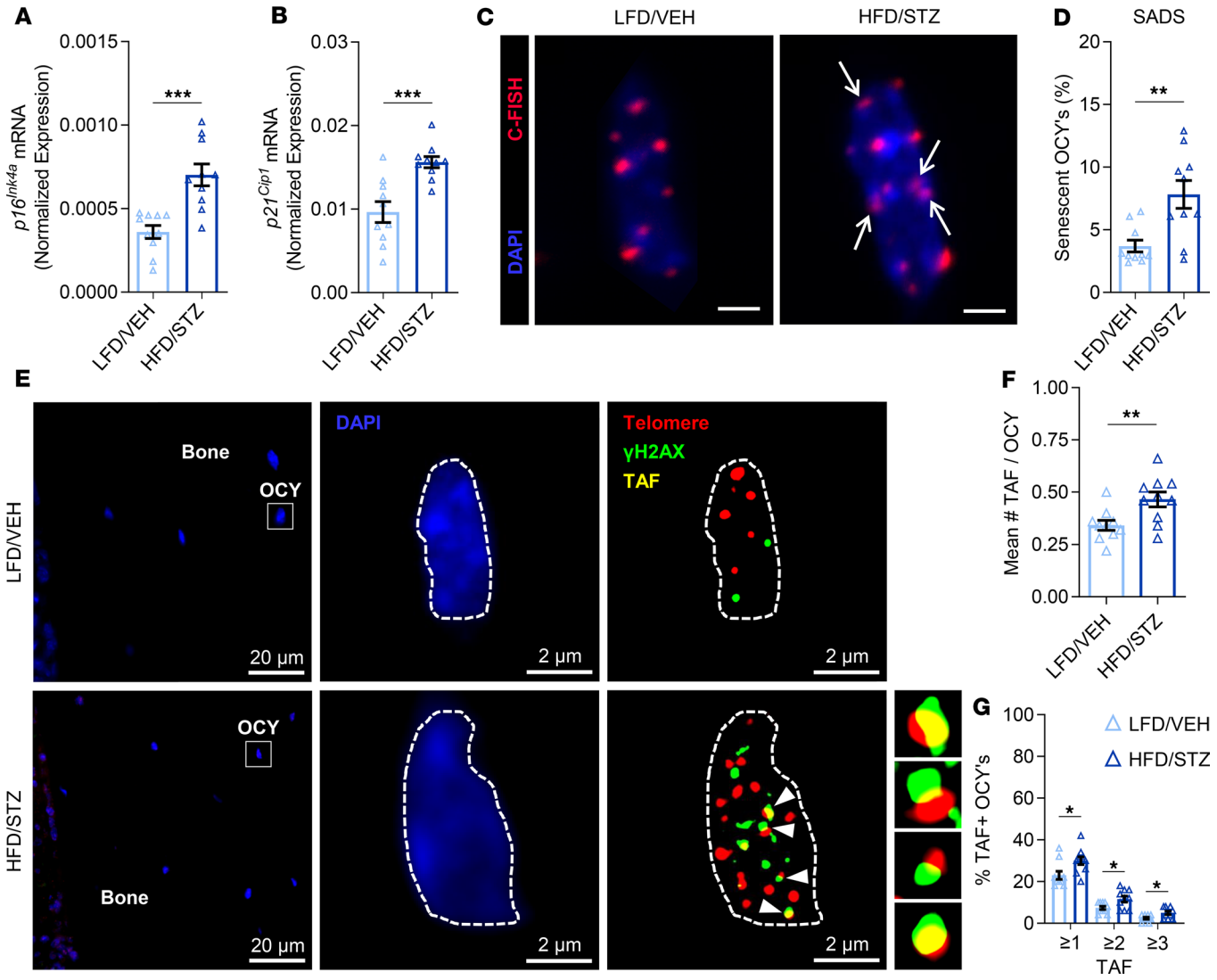

Figure 7. T2D is associated with accelerated osteocyte senescence in bone. In vivo rt-qPCR mRNA gene expression analyses of (**A**) *p16*^{Ink4a} (*Cdkn2a*) and (**B**) *p21*^{Cip1} (*Cdkn1a*) in osteocyte-enriched bone samples. (**C**) Representative images of a nonsenescent osteocyte in an LFD/VEH mouse (original magnification, ×100) versus a senescent osteocyte in an HFD/STZ mouse according to the senescence-associated distension of satellites (SADS, see white arrows) assay in cortical bone diaphysis sections (scale bars: 2 µm); 30 osteocytes were analyzed per mouse (n = 10/group). C-FISH, centromere-FISH. (**D**) Quantification of the percentage of senescent osteocytes in mice according to the SADS assay. (**E**) Representative images of bone and within a nonsenescent osteocyte in an LFD/VEH mouse (original magnification, ×63, oil) versus a senescent osteocyte in an HFD/STZ mouse according to the telomere-associated foci (TAF, see white arrows) assay in cortical bone diaphysis sections; 50 osteocytes were analyzed per mouse (n = 10/group). Quantification of (**F**) the mean number of TAF per osteocyte and (**G**) the mean percentage of TAF-positive osteocytes per mouse based on the following criteria: percentage of OCYs with ≥1 TAF, percentage of OCYs with ≥2 TAF, and percentage of OCYs with ≥3 TAF, respectively. Data represent mean ± SEM (error bars). *P < 0.05; **P < 0.01; ***P < 0.001 (independent samples t test or Wilcoxon's rank-sum test, as appropriate). HFD, high-fat diet; STZ, streptozotocin; T2D, type 2 diabetes; LFD, low-fat diet; VEH, vehicle; OCY's, osteocytes.

Discussion

The worldwide prevalence of T2D is increasing dramatically (30). When left uncontrolled, T2D can cause multiorgan dysfunction, including renal failure, blindness, amputations, and cardiovascular disease (31). Furthermore, over the past decade or so, it has become increasingly clear that T2D also causes skeletal complications (8, 9). Indeed, fracture risk is higher in patients with T2D who paradoxically often present clinically with normal or higher BMD (6, 7); notwithstanding, bone turnover in these individuals is altered and their bone quality is impaired, perhaps due to the accumulation of AGEs and inflammatory factors in bone that impair its quality (9). Despite this knowledge, the pathophysiological mechanisms underlying skeletal dysfunction in T2D are not well understood. Indeed, how accelerated skeletal fragility is caused in T2D has been an important, open question in the fields of bone biology and diabetes (32). To begin

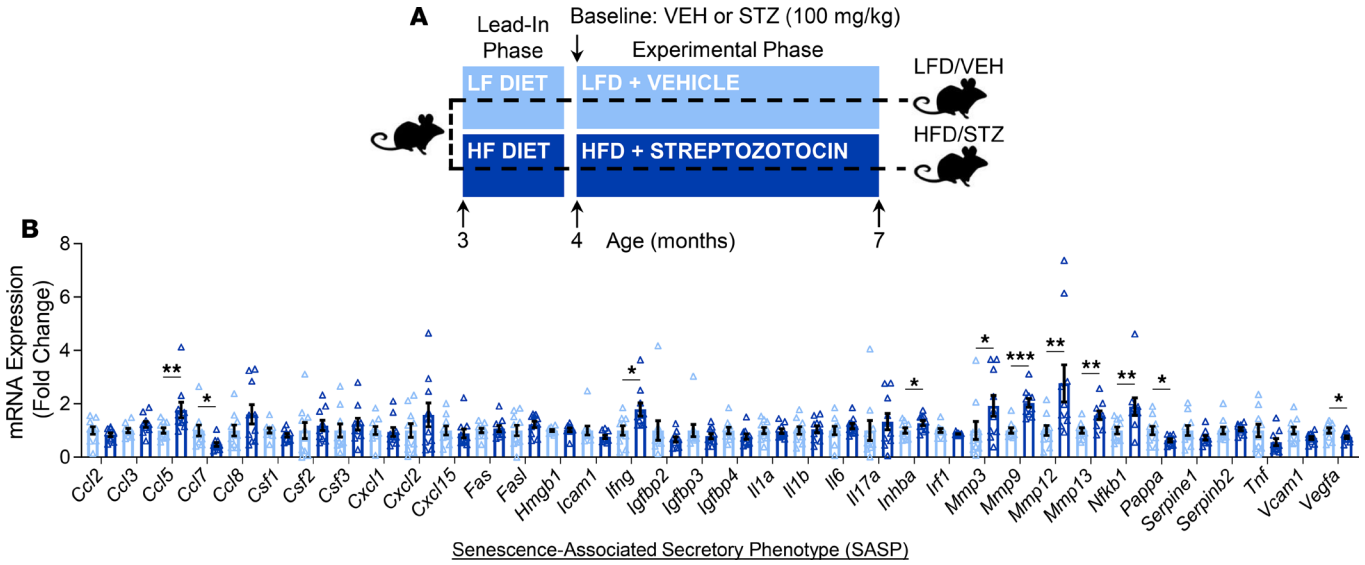

Figure 8. T2D is associated with the development of a unique SASP in bone. (**A**) Schematic of the study design depicting male C57BL/6 mice randomized to either LFD (10% kcal from fat) or HFD (60% kcal from fat) for 1 month (lead-in phase) followed by treatment (at baseline) with either VEH or STZ and follow-up for 3 months (experimental phase) out to 7 months of age (endpoint): LFD/VEH, HFD/STZ (n = 10/group). (**B**) In vivo T2D-associated fold changes in rt-qPCR mRNA gene expression of 36 established SASP factors in bone samples of mice. Data represent mean ± SEM (error bars). $^{*}P < 0.05$; $^{**}P < 0.01$; $^{***}P < 0.001$ (independent samples t test or Wilcoxon's rank-sum test, as appropriate). HFD, high-fat diet; STZ, streptozotocin; T2D, type 2 diabetes; LFD, low-fat diet; VEH, vehicle; OCY's, osteocytes; SASP, senescence-associated secretory phenotype.

to answer this question, a major goal is to develop appropriate animal models of T2D that mimic (at least most of) the key metabolic and skeletal pathophysiological characteristics of human adult-onset T2D, based on the idea that the closer these models can come to sharing the key features of T2D in humans, the more significant and impactful they would be for basic and translational research. Multiple rodent models have been proposed for this purpose, and while no single model can be perfect, a recent thorough review of commonly used rodent models concluded that most have significant limitations (10). Thus, developing an optimal model of adult-onset T2D-induced skeletal fragility would be an important step toward identifying novel approaches to treat diabetic bone disease.

In the current study, we utilized a nongenetic mouse model mimicking human adult-onset T2D in the setting of obesity that displays overt hyperglycemia, dysfunctional insulin secretion, insulin resistance, and β cell deterioration — i.e., the HFD/STZ mouse model of T2D (17–19). A significant advantage of this model for studying the effects of T2D on bone is that the onset of diabetes occurs during adulthood, in an inducible manner, as opposed to most previously studied rodent models, in which T2D onset occurs before skeletal maturation (10). Importantly, in the setting of HFD feeding, this inducible feature allows us to attain both environmental (in obesity) as well as temporal (in the adult mouse) control of T2D onset, which closely mimics the most common onset of T2D in humans. It is perhaps surprising that, despite representing one of the models of choice by many in the diabetes field (33), to our knowledge, the skeletal phenotype of HFD/STZ mice has not been rigorously characterized. Here, we show in C57BL/6 male mice that a onetime pharmacological intervention (STZ) initiated in young adulthood combined with HFD-induced obesity causes hallmark features of T2D, consistent with previous studies (17–19), including prolonged hyperglycemia, insulin resistance, and pancreatic β cell dysfunction, but not complete destruction. In contrast, neither intervention alone (STZ or HFD) was sufficient to cause diabetes or hyperglycemia. In addition, HFD/STZ (i.e., T2D) caused several changes in bone quality that closely mirrored those observed in humans with T2D. These alterations included impaired trabecular/cortical bone microarchitecture, deficits in directly measured biomechanical properties of bone strength at axial and appendicular skeletal sites, impaired indices of bone material properties, altered bone turnover, and elevated levels of the AGE CML in both bone and blood. Furthermore, T2D initiated during young adulthood caused the premature accumulation of senescent osteocytes in bone with a unique proinflammatory SASP signature. Thus, our data are consistent with previous reports implicating T2D in the pathogenesis of skeletal fragility (as reviewed in ref. 9), potentially via upregulation of AGEs and activation of the

RAGE signaling pathway. Further, we identify, for the first time to our knowledge, accelerated cellular senescence as a potential mediator that, in addition to the RAGE pathway, warrants further study.

We chose to use the HFD/STZ mouse model of T2D (17–19) for this study based on the following rationale: (a) the mouse is amenable to in-depth tissue, cellular, and molecular analyses; (b) mice are easier to obtain and more cost-effective to maintain than rats; (c) the ability to induce adult-onset T2D in the setting of obesity, which mimics the majority of human cases, is an advantage over spontaneous or pre–skeletally mature models; (d) the relatively fast induction period permits shorter duration studies as compared with studies in larger, nonrodent species; and (e) this model has been used extensively in the diabetes field, over multiple decades, and although it can be debated which model is the ideal, the HFD/STZ model has withstood the test of time as it is still widely used and considered by many to be the model of choice for studying the pathophysiology of T2D and evaluating therapeutic compounds for treatment of T2D. We do, however, recognize that no rodent model will ever recapitulate every feature of human diabetic skeletal fragility because there are unavoidable differences between humans and rodents. For example, under physiological conditions rodents lack Haversian remodeling and therefore do not develop intracortical porosity, which has been reported to be higher in humans with T2D relative to nondiabetic controls (34, 35). However, it should be emphasized that cortical vBMD (as assessed by in vivo longitudinal μCT scanning at the tibia diaphysis in our study) was significantly reduced in HFD/STZ (i.e., T2D) mice as compared with control mice ($P < 0.001$). Thus, cortical vBMD, which has also been reported to be lower in humans with T2D (35), may be a useful surrogate for cortical bone quality in mice. Therefore, when all these issues are considered, we believe the HFD/STZ mouse model offers significant advantages for studying T2D-associated skeletal fragility.

The underlying pathophysiological mechanisms driving metabolic dysfunction and skeletal fragility in T2D are complex and still need to be better understood, although activation of the RAGE signaling pathway (20) and the accumulation of AGEs in multiple tissues, including bone, have been hypothesized as central mediators (9). Indeed, particularly with prolonged periods of uncontrolled hyperglycemia and during later, more advanced stages of T2D, glucose toxicity contributes to higher levels of AGEs that activate RAGE signaling in various cell types, including those of the osteoblast and myeloid lineages (36, 37), contributing to a proinflammatory bone microenvironment that fuels osteoclastogenesis and increased bone resorption (38). This may, at least in part, explain the increased levels of NF-κB (a downstream effector in the RAGE pathway) (20) and RANKL (a protein central to bone resorption because it binds RANK on the surfaces of osteoclast precursors to trigger osteoclastogenesis) (39), which were both detected in bone samples of HFD/STZ mice. These data also fit with the higher levels of osteoclasts revealed by histomorphometry on the endocortical bone surfaces of HFD/STZ mice as well as the higher circulating levels of the bone resorption marker, CTx, detected in these animals. By contrast, we observed no changes in osteoblasts or P1NP in bone or blood, respectively, although decreases in these parameters, as suggested by some studies in humans with T2D (40, 41), may require a longer duration of disease or greater severity. Nevertheless, despite the relatively short experimental phase of our study (12 weeks), HFD/STZ mice did, in fact, display significant (albeit in some cases modest; $P > 0.05$) reductions in directly measured bone biomechanical properties, indices of bone material properties, and direct measures of bone strength. It should be noted, however, that bone material properties in HFD/STZ mice were affected more at appendicular (i.e., femur) relative to axial (i.e., spine) skeletal sites. This might reflect the greater propensity for T2D to affect skeletal sites predominantly composed of cortical versus trabecular bone, as also tends to be the case in humans (34). In addition, HFD/STZ mice displayed significantly reduced ($P < 0.05$) bone formation levels as assessed by dynamic histomorphometry. We would, however, expect that with a longer study duration (at later stages of T2D) when insulin, which is bone anabolic (42), becomes more deficient, bone formation may be reduced even further. In addition, AGEs are also thought to suppress bone formation by directly impairing osteoblast functions (36), which again is consistent with our histomorphometry data demonstrating lower mineral apposition and bone formation rates on endocortical bone surfaces of HFD/STZ mice. Whether these as well as other changes (e.g., deficits in bone quality) in response to T2D would become even more dramatic with longer disease duration in HFD/STZ mice needs to be tested in future studies.

An advantage of our study was in leveraging LC-MS/MS to accurately assess AGEs, including pentosidine and CML, in bone tissue and blood samples. Pentosidine is one of the most commonly reported AGEs (typically assessed by commercial immunoassays) in clinical studies that have examined correlations between AGEs and bone parameters in patients with T2D and nondiabetic subjects (43, 44). However, we

did not observe similar findings in our mouse model of T2D. This may be related to several limitations of the earlier reported commercial immunoassays, including lack of specificity by detecting nonspecific isoforms or fragments of pentosidine. Furthermore, although these studies have reported higher levels of pentosidine in biological samples, including blood and urine, from subjects with T2D as compared with nondiabetic controls, these findings have not been verified by mass spectrometry or in bone tissue samples. Furthermore, recent work using mass spectrometry has demonstrated that pentosidine accounts for only a small fraction of possible fluorescent AGEs (45). Consistent with this, our LC-MS/MS assay detected relatively low levels of pentosidine in both blood and bone samples of control and T2D mice. In contrast, levels of CML, a dominant component of total nonfluorescent AGEs (25), were found by our LC-MS/MS assay to be significantly higher in both blood and bone tissue samples of T2D relative to control mice and were even further elevated in these tissues obtained from old mice. Interestingly, when CML accumulates on proteins such as collagen in bone, it adversely affects the overall biophysical properties and functions of the tissue (46, 47). Consistent with our data in mice with T2D, our recent study in a cohort of nondiabetic control (n = 49) versus T2D (n = 95; HbA1c level ≥ 6.5%, diagnosis for at least 5 years) subjects, including women and men at least 50 years old, demonstrated using LC-MS/MS that blood levels of CML, but not pentosidine, were significantly elevated in humans with T2D and that CML was associated with glycemic control, as assessed by HbA1c (48). Therefore, in both mice and humans CML may represent a viable surrogate measure of the overall AGE burden in various disease states, including T2D, although additional supporting evidence is needed to confirm this premise.

T2D in the setting of obesity is a complex disorder and an associated major risk factor for a range of comorbidities and health problems (31), although the mechanistic basis linking these conditions in humans with T2D is incompletely understood. Interestingly, however, cellular senescence has been hypothesized not only as a key driver of aging in several tissues (21), including in old bone (as reviewed in refs. 49, 50) but also as a driver of conditions of "accelerated" aging, such as T2D (51). In addition to acquiring an oftentimes complex SASP, senescent cells can display a variety of biomarkers, including profound changes in heterochromatin (i.e., SADS) (27), DNA damage colocalized with telomeres (i.e., TAF) (28), and increased expression of the cyclin-dependent kinase inhibitors $p16^{Ink4a}$ and $p21^{Cip1}$ (21). Accelerated accumulation of senescent cells has been identified in mice during obesity in adipose tissue, liver, and brain (13–15) and with T2D in the pancreas (e.g., senescent β cells) (16). In the latter study, HFD-induced obesity and insulin resistance in mice caused accelerated β cell senescence with a specific SASP, whereas senolysis (i.e., clearance of senescent cells) using either genetic or pharmacological approaches improved glucose homeostasis, β cell function, and the gene expression profile of β cells (16). However, whether there is a direct causal relationship between cellular senescence and skeletal fragility in T2D has not been established. Here, we showed in mice with T2D that at least a subset of osteocytes in bone display features of cellular senescence, including upregulated expression of $p16^{Ink4a}$ and $p21^{Cip1}$ and increased SADS (27) and TAF (28), and acquire a unique SASP profile characterized by increased levels of *NfKB* as well as a group of matrix-degrading metalloproteinases (i.e., *Mmp3*, *Mmp9*, *Mmp12*, and *Mmp13*) that together, in combination with enhanced RAGE signaling, as discussed above, may contribute to impaired bone quality in T2D. This hypothesis needs to be tested in future studies.

The relationship between fat and bone is complex, and defining the contribution of obesity to skeletal health in nondiabetic individuals is challenging because of the interplay among factors that favor versus those that are detrimental to bone (52). Although the skeletal phenotype of HFD-induced obesity in mice has been studied extensively (as reviewed in ref. 10), with mixed agreement on the trabecular and cortical phenotypes of these animals, data from our study suggest that HFD-induced obesity alone has lesser effects on bone microarchitecture and quality as compared with T2D. Thus, the bone abnormalities in HFD/STZ mice may be driven by persistent hyperglycemia, and the resultant downstream effects on RAGE signaling and cellular senescence, rather than effects of HFD alone, such as hyperlipidemia and insulin resistance, although larger sample sizes will be required to confirm this premise. Indeed, our study was not sufficiently powered to rigorously dissect the effects of obesity versus T2D on bone or on additional outcomes, such as cellular senescence and SASP. As such, we focused the more in-depth analyses on the control (LFD/VEH) and T2D (HFD/STZ) groups. Another potential limitation of our study was the relatively short duration of T2D (i.e., 12 weeks), which may at least in part explain why some the effects of T2D we observed on, for example, aspects of bone quality were less dramatic as compared with those observed by μCT. Nevertheless, the latter data provide clear evidence that there are detrimental effects of T2D on bone microarchitecture and geometry, particularly at cortical skeletal sites. Whether effects on aspects of bone quality

in T2D mice would have been more dramatic following longer duration of T2D, which often is the case in humans, warrants further study.

In summary, the combination of HFD/STZ initiated during adulthood in mice caused several key features of adult-onset T2D as well as changes in bone quality that closely mirrored those previously reported in the human diabetic skeleton. Importantly, this is likely the first rigorous skeletal characterization of an obese mouse model that develops adult-onset T2D, in an inducible manner, after skeletal maturity. The skeletal alterations found in HFD/STZ mice with T2D included impaired trabecular/cortical bone microarchitecture, deficits in directly measured biomechanical properties of bone strength at axial and appendicular skeletal sites, impaired indices of bone material properties, altered bone turnover, and elevated levels of the AGE CML in both bone and blood. In addition, T2D caused the premature accumulation of senescent osteocytes in bone with a unique proinflammatory SASP signature. These findings thus establish the RAGE pathway and senescent cells as hallmarks of bone fragility in T2D and highlight HFD/STZ mice as a useful model both in future mechanistic studies examining the underlying causes of diabetic bone dysfunction and for evaluating novel therapeutic approaches to treat T2D-associated skeletal fragility.

Methods

General experimental approaches. Animals were randomized to diets and treatment groups as indicated below. Experiments, assessments, and analyses were performed in a blinded fashion. No mice, samples, or data points were excluded from the reported analyses.

Animals. As specified here and in the figure legends, male C57BL/6 mice (n = 10/group) were studied because in this background, males are much more susceptible to T2D induced by HFD/STZ; indeed, previous work has established that male C57BL/6 mice develop obesity sooner in response to HFD (53–55), and when combined with a single, relatively low dose of STZ (see below), their insulin resistance and glucose intolerance are more pronounced as compared with females (17–19). Thus, as justified scientifically, we used young-adult (starting at 3 months, ending at 7 months of age) C57BL/6 male WT mice for this study (n = 10/group). To compare T2D mice with natural, chronological aging, "old" (24-month) male C57BL/6 WT mice were obtained from the National Institute on Aging breeding colony. All mice were housed in ventilated cages and maintained within a pathogen-free, accredited facility under a 12-hour light/12-hour dark cycle with constant temperature (23°C) and access to food (diet details are specified below) and water ad libitum. Animal studies were performed under protocols approved by the Institutional Animal Care and Use Committee (IACUC), and experiments were performed in accordance with Mayo Clinic IACUC guidelines. All assessments were performed in a blinded fashion.

Study design, diets, treatments, and generation of the T2D mouse model. A schematic of the study design depicting the 2 phases of the study (lead-in and experimental), the 4 group categories, and the timeline for the diets/treatments is shown in Figure 1A. Male 3-month-old C57BL/6 WT mice of comparable mean body weights were randomized to 4 weeks (lead-in phase) of either LFD (D12450J) or HFD (D12492) (Research Diets); note that the sucrose content is kept constant in both diets, whereas the percentage of kilocalories from fat differs (LFD = 10%, HFD = 60%). The composition of the diets is provided in Supplemental Table 1. After 4 weeks on the diet (lead-in phase), baseline measurements were performed (as detailed in the sections below) on all mice at 4 months of age. After the lead-in phase of diet acclimation and baseline measurements, the 4-month-old mice were then secondarily randomized to a single dose, injected intraperitoneally, of either VEH (50 mM sodium citrate buffer, pH 4.5) or STZ (100 mg/kg dissolved in VEH, MilliporeSigma) and kept on the same diet for the following 12 weeks (experimental phase). Importantly, this dose of STZ does not cause diabetes in LFD- or chow-fed mice (17–19). In contrast, and consistent with our data (see Results), previous studies have established that in the setting of HFD-induced obesity, this dose of STZ causes several features of T2D, including hyperglycemia, defects in insulin sensitivity and secretion, and reduced pancreatic β cell mass/capacity (17–19). Following the 4-week lead-in phase (LFD or HFD) and the single-dose treatment (VEH or STZ), mice in each of the 4 groups (LFD/VEH n = 10; LFD/STZ n = 10; HFD/VEH n = 10; HFD/STZ n = 10) were, as noted above, kept on their randomized diet for an additional 12 weeks (experimental phase), after which endpoint measurements were performed, followed by euthanasia and tissue harvesting. Thus, all mice were 7 months of age at necropsy (i.e., 1 month of lead-in phase, 3 months of experimental phase). During the 12-week experimental phase, nonfasted glucose measurements were obtained weekly, at the same time of day, from blood (taken by nicking the distal part of the tail) using a FreeStyle Lite glucose monitor (Cardinal Health Pharmacy).

HFD/STZ mice with median glucose levels more than 250 mg/dL between 2 and 12 weeks after STZ injection were included in the T2D group, in accordance with previous criteria for the diagnosis of T2D in mice (17–19). Importantly, this definition of T2D in C57BL/6 mice is common throughout the diabetes and skeletal literature (10, 22). HFD/STZ (i.e., T2D) mice not reaching median glucose levels more than 250 mg/dL by 6 weeks post-STZ did not continue in the study. As shown in Results, each of the 3 other groups (i.e., LFD/VEH, LFD/STZ, and HFD/VEH) consistently had glucose values less than 200 mg/dL throughout the study. In addition to glucose, nonfasted measurements of HbA1c (percentage) and insulin (nanograms/milliliter) were obtained from tail blood and lateral saphenous vein plasma, respectively, at baseline, midpoint, and endpoint of the experimental phase, as detailed below (see *Biochemical assays*).

Mouse assessments of body composition. Body mass (grams) was recorded on all mice at the onset of the lead-in phase (age 3 months) and at baseline (age 4 months), midpoint (age 5.5 months), and endpoint (age 7 months) of the experimental phase. At baseline and endpoint of the experimental phase, body composition (i.e., whole-body lean grams and fat mass grams) was assessed in vivo using quantitative Echo magnetic resonance imaging (EchoMRI-100) in mice that were nonanesthetized and conscious, as described (56).

Mouse tissue collection and assessments. Prior to sacrifice, body mass (grams) was recorded and serum was collected in the morning (under nonfasting conditions) from anesthetized mice via cardiac puncture and stored at –80°C. After euthanasia, the tibiae, femurs, humeri, and vertebrae were excised from the mice and skeletal muscle/connective tissues were removed. The right femur was stored in gauze soaked with 0.9% saline (NaCl) at –20°C for direct biomechanical strength testing by 3-point bending (see *Three-point bend testing*). The left femur was stored in saline-soaked gauze at –20°C for biomaterial RPI testing (see *RPI testing*). A portion of the lumbar vertebrae ($L_{3–4}$) was stored in saline-soaked gauze at –20°C for biomechanical *Compression load testing* and biomaterial *Nanoindentation testing*, as detailed below. The right tibia and part of the lumbar vertebrae ($L_{5–6}$) were fixed in ethanol (EtOH) before ex vivo μCT scanning (see *Skeletal imaging*). After scanning and image analysis, the nondecalcified right tibia was embedded in methyl methacrylate and sectioned for histomorphometry, immunohistochemistry (see *Skeletal histomorphometry assessments*), and FISH (see *SADS analysis of osteocytes*). The left tibia was used to generate an osteocyte-enriched cortical bone sample prepared by cutting the metaphyses, flushing the bone marrow from the diaphysis with FACS buffer, followed by centrifuging to remove bone marrow elements. The remaining osteocyte-enriched samples were immediately homogenized in QIAzol Lysis Reagent (QIAGEN) and frozen at –80°C for rt-qPCR mRNA gene expression analyses (see *rt-qPCR analysis*). Soft tissues were excised from the humeri and thoracic vertebrae, which were subsequently centrifuged to remove bone marrow and then decalcified in DeCal HCl/EDTA solution (StatLab) for 24 hours. Complete decalcification was verified using dual-energy x-ray absorptiometry with the Lunar PIXImus densitometer (software version 1.44.005; Lunar Corp.), as defined by a BMD of 0.00 g/cm^2. Decalcified bones were crushed to powder under liquid N_2 and stored at –80°C for analysis of AGEs (see *Quantification of AGEs*). Finally, the pancreas was fixed in formalin for 24 hours and subsequently stored in 100% EtOH for quantifying β cell area (see *Immunofluorescence analysis of pancreatic islet cells*).

Skeletal imaging. All imaging and analysis were performed in a blinded fashion as described by our group previously (11, 12, 56) and as detailed in Supplemental Methods.

Compression load testing. Tests of compression loading were performed in a blinded fashion as described by our group previously (12) and as detailed in Supplemental Methods.

Three-point bend testing. Details regarding the particulars of the 3-point bend testing are provided in Supplemental Methods.

Nanoindentation testing. Nanoindentation testing was performed in a blinded fashion as described previously by our group (12) and as detailed in Supplemental Methods.

RPI testing. Details regards the particulars of the RPI testing are provided in Supplemental Methods.

Skeletal histomorphometry assessments. All bone histomorphometry analyses were performed in blinded fashion as previously described by our group (12) and as detailed in Supplemental Methods.

Immunofluorescence analysis of pancreatic islet cells. As described (57), pancreata were processed and embedded in paraffin using an Excelsior ES Tissue Processor and a HistoStar Embedding Workstation (Thermo Fisher Scientific); 0.4 μm sections were cut using an HM 325 Rotary Microtome (Thermo Fisher Scientific). For quantification of β cell area, paraffin-embedded pancreatic sections were stained with DAPI and for insulin (ab7842, 1:100; Abcam). All slides were viewed, imaged, and analyzed using a Zeiss Axio Observer Z1 microscope (Carl Zeiss Microscopy, LLC) and ZenPro software (Carl Zeiss Microscopy, LLC).

Biochemical assays. All biochemical assays were performed in blinded fashion, as detailed in Supplemental Methods.

Quantification of AGEs. Measures of AGEs, including CML and pentosidine in bone tissue and in nonfasted circulating serum samples, were performed using mass spectrometry as detailed in Supplemental Methods.

rt-qPCR analysis. Details for the rt-qPCR procedures and analyses are provided in Supplemental Methods.

SADS analysis of osteocytes. Detailed procedures for the SADS assay are provided in Supplemental Methods.

TAF analysis of osteocytes. To measure cellular senescence in osteocytes of the diaphyseal cortex, the TAF assay (n = 10/group) was performed on murine right tibia nondecalcified methyl methacrylate–embedded sections. Our protocol was adapted from a previous study (28). Bone sections were deplasticized and hydrated in EtOH gradient followed by water and PBS. Antigen was retrieved by incubation in Tris-EDTA (pH 9.0) at 95°C for 15 minutes. After cooldown and hydration with water and PBS (0.5% Tween-20/0.1% Triton X-100), slides were placed in blocking buffer (1:60 normal goat serum; Vector Laboratories; S-1000; in 0.1% BSA/PBS) for 30 minutes at room temperature (RT). Primary antibody γ-H2AX (1:200; anti–γ-H2A.X rabbit monoclonal antibody, Cell Signaling Technology; 9718) was diluted in blocking buffer and incubated overnight at 4°C. The next day, slides were washed with PBS (0.5% Tween-20/0.1% Triton X-100) followed by PBS alone and then incubated for 30 minutes with secondary goat, anti-rabbit antibody biotinylated (1:200; Vector Laboratories; BA-1000) in blocking buffer. Subsequently, slides were washed with PBS (0.5% Tween-20/0.1% Triton X-100) followed by PBS alone, then incubated for 60 minutes with tertiary antibody (1:500; Cy5 Streptavidin, Vector Laboratories; SA-1500) in PBS. Slides were then washed 3 times with PBS, followed by FISH for TAF detection. Briefly, following 4% paraformaldehyde cross-linking for 20 minutes, sections were washed 3 times (5 minutes each in PBS) and dehydrated in graded (70%, 90%, and 100%, 3 minutes each) ice-cold EtOH. Sections were then dried and denatured for 10 minutes at 80°C in hybridization buffer: 0.1 M Tris (pH 7.2), 25 mM $MgCl_2$, 70% formamide (MilliporeSigma), 5% blocking reagent (Roche), with 1.0 μg/mL of Cy3-labeled telomere-specific (CCCTAA) peptide nucleic acid probe (TelC-Cy3, Panagene Inc.; F1002), followed by humidified dark room hybridization for 2 hours at RT. Sections were then washed and mounted with VECTASHIELD DAPI-containing mounting medium (Life Technologies) before image acquisition and analysis. The number of TAF per osteocyte was quantified in a blinded fashion by examining overlap of signals from the telomere probe with γ-H2AX (i.e., phosphorylation of the C-terminal end of histone H2A.X — a marker of double-strand breaks in DNA). The mean number of TAF per osteocyte in cortical bone diaphyses was quantified using FIJI (an ImageJ distribution software; NIH, https://imagej.nih.gov/ij/), and the percentage of TAF^+ OCYs was calculated for each mouse based on the following criteria: percentage of OCYs with ≥1 TAF, percentage of OCYs with ≥2 TAF, and percentage of OCYs with ≥3 TAF.

Statistics. Graphical data are shown as means ± SEM unless otherwise specified. Sample sizes, determined based on pilot or previously conducted and published experiments (e.g., Farr et al., refs. 11, 12) in which statistically significant differences were observed among various bone parameters in response to multiple interventions in our laboratory, are indicated in the figure legends; all samples presented represent biological replicates. No mice, samples, or data points were excluded from analyses. Data were examined for normality and distribution using dot plots and histograms; all variables were examined for skewness and kurtosis. If the normality or equal-variance assumptions for parametric analysis methods were not met, data were analyzed using nonparametric tests (e.g., Wilcoxon's rank-sum test). For parametric tests, depending on the comparison, differences between groups were analyzed by 2-tailed independent samples t test or 1-way ANOVA, where justified as appropriate (see figure legends). When ANOVA determined a statistically significant ($P < 0.05$) effect, pairwise multiple comparisons were performed and the Tukey post hoc method was applied. Statistical analyses were performed using either GraphPad Prism (Version 8.0) or the Statistical Package for the Social Sciences for Windows, Version 25.0 (SPSS, Chicago, IL). A P value less than 0.05 (2 tailed) was considered statistically significant.

Study approval. Animal studies were performed under protocols approved by the IACUC, and experiments were performed in accordance with Mayo Clinic IACUC guidelines.

Author contributions

JNF conceived and directed the project. JNF designed the experiments and interpreted the data with input from RJS, JFP, AV, AVM, SK, and DGM. Experiments were performed by BAE, JLR, BST, DGF, KLO, OPB, JMH, ART, RK, and ABL. JNF wrote the manuscript. All authors reviewed the manuscript. JNF oversaw all experimental design, data analyses, and manuscript preparation. JNF accepts responsibility for the integrity of the data analysis.

Acknowledgments

This work was supported by NIH grants P01 AG062413 (to JNF, SK), R21 AG065868 (to JNF, SK), K01 AR070241 (to JNF), and R01 AR068275 (to DGM) and both a High-Risk Pilot Award (to JNF) and a Career Development Award (to JNF) from the Mayo Clinic Robert and Arlene Kogod Center on Aging, as well as the Richard F. Emslander Career Development Award in Endocrinology (to JNF).

Address correspondence to: Joshua N. Farr, Guggenheim 7-11D, Mayo Clinic College of Medicine, 200 First Street SW, Rochester, Minnesota 55905, USA. Phone: 507.538.0085; Email: farr.joshua@mayo.edu.

1. Taylor SI. Deconstructing type 2 diabetes. *Cell*. 1999;97(1):9–12.
2. Bell GI, Polonsky KS. Diabetes mellitus and genetically programmed defects in beta-cell function. *Nature*. 2001;414(6865):788–791.
3. Cavaghan MK, Ehrmann DA, Polonsky KS. Interactions between insulin resistance and insulin secretion in the development of glucose intolerance. *J Clin Invest*. 2000;106(3):329–333.
4. Kahn BB. Type 2 diabetes: when insulin secretion fails to compensate for insulin resistance. *Cell*. 1998;92(5):593–596.
5. Butler AE, Janson J, Bonner-Weir S, Ritzel R, Rizza RA, Butler PC. Beta-cell deficit and increased beta-cell apoptosis in humans with type 2 diabetes. *Diabetes*. 2003;52(1):102–110.
6. Ma L, et al. Association between bone mineral density and type 2 diabetes mellitus: a meta-analysis of observational studies. *Eur J Epidemiol*. 2012;27(5):319–332.
7. Bonds DE, et al. Risk of fracture in women with type 2 diabetes: the Women's Health Initiative Observational Study. *J Clin Endocrinol Metab*. 2006;91(9):3404–3410.
8. Farr JN, Khosla S. Determinants of bone strength and quality in diabetes mellitus in humans. *Bone*. 2016;82:28–34.
9. Napoli N, et al. Mechanisms of diabetes mellitus-induced bone fragility. *Nat Rev Endocrinol*. 2017;13(4):208–219.
10. Fajardo RJ, Karim L, Calley VI, Bouxsein ML. A review of rodent models of type 2 diabetic skeletal fragility. *J Bone Miner Res*. 2014;29(5):1025–1040.
11. Farr JN, et al. Identification of senescent cells in the bone microenvironment. *J Bone Miner Res*. 2016;31(11):1920–1929.
12. Farr JN, et al. Targeting cellular senescence prevents age-related bone loss in mice. *Nat Med*. 2017;23(9):1072–1079.
13. Schafer MJ, et al. Exercise prevents diet-induced cellular senescence in adipose tissue. *Diabetes*. 2016;65(6):1606–1615.
14. Palmer AK, et al. Targeting senescent cells alleviates obesity-induced metabolic dysfunction. *Aging Cell*. 2019;18(3):e12950.
15. Ogrodnik M, et al. Obesity-induced cellular senescence drives anxiety and impairs neurogenesis. *Cell Metab*. 2019;29(5):1061–1077.e8.
16. Aguayo-Mazzucato C, et al. Acceleration of β cell aging determines diabetes and senolysis improves disease outcomes. *Cell Metab*. 2019;30(1):129–142.e4.
17. Luo J, et al. Nongenetic mouse models of non-insulin-dependent diabetes mellitus. *Metab Clin Exp*. 1998;47(6):663–668.
18. Mu J, et al. Chronic inhibition of dipeptidyl peptidase-4 with a sitagliptin analog preserves pancreatic beta-cell mass and function in a rodent model of type 2 diabetes. *Diabetes*. 2006;55(6):1695–1704.
19. Mu J, et al. Inhibition of DPP-4 with sitagliptin improves glycemic control and restores islet cell mass and function in a rodent model of type 2 diabetes. *Eur J Pharmacol*. 2009;623(1-3):148–154.
20. Litwinoff E, Hurtado Del Pozo C, Ramasamy R, Schmidt AM. Emerging targets for therapeutic development in diabetes and its complications: the RAGE signaling pathway. *Clin Pharmacol Ther*. 2015;98(2):135–144.
21. Tchkonia T, Zhu Y, van Deursen J, Campisi J, Kirkland JL. Cellular senescence and the senescent secretory phenotype: therapeutic opportunities. *J Clin Invest*. 2013;123(3):966–972.
22. Kleinert M, et al. Animal models of obesity and diabetes mellitus. *Nat Rev Endocrinol*. 2018;14(3):140–162.
23. Dyer DG, et al. Accumulation of Maillard reaction products in skin collagen in diabetes and aging. *J Clin Invest*. 1993;91(6):2463–2469.
24. Schleicher ED, Wagner E, Nerlich AG. Increased accumulation of the glycoxidation product N(epsilon)-(carboxymethyl)lysine in human tissues in diabetes and aging. *J Clin Invest*. 1997;99(3):457–468.
25. Reddy S, Bichler J, Wells-Knecht KJ, Thorpe SR, Baynes JW. N epsilon-(carboxymethyl)lysine is a dominant advanced glycation end product (AGE) antigen in tissue proteins. *Biochemistry*. 1995;34(34):10872–10878.
26. Grandhee SK, Monnier VM. Mechanism of formation of the Maillard protein cross-link pentosidine. Glucose, fructose, and ascorbate as pentosidine precursors. *J Biol Chem*. 1991;266(18):11649–11653.
27. Swanson EC, Manning B, Zhang H, Lawrence JB. Higher-order unfolding of satellite heterochromatin is a consistent and early event in cell senescence. *J Cell Biol*. 2013;203(6):929–942.
28. Hewitt G, et al. Telomeres are favoured targets of a persistent DNA damage response in ageing and stress-induced senescence. *Nat Commun*. 2012;3:708.
29. Coppé JP, et al. Senescence-associated secretory phenotypes reveal cell-nonautonomous functions of oncogenic RAS and the p53 tumor suppressor. *PLoS Biol*. 2008;6(12):2853–2868.
30. NCD Risk Factor Collaboration (NCD-RisC). Worldwide trends in diabetes since 1980: a pooled analysis of 751 population-based studies with 4.4 million participants. *Lancet*. 2016;387(10027):1513–1530.
31. DeFronzo RA, et al. Type 2 diabetes mellitus. *Nat Rev Dis Primers*. 2015;1:15019.
32. Dhaliwal R, Rosen CJ. Type 2 diabetes and aging: a not so sweet scenario for bone. *Horm Metab Res*. 2016;48(11):771–778.
33. Furman BL. Streptozotocin-induced diabetic models in mice and rats. *Curr Protoc Pharmacol*. 2015;70:5.47.1–5.47.20.
34. Burghardt AJ, et al. High-resolution peripheral quantitative computed tomographic imaging of cortical and trabecular bone microarchitecture in patients with type 2 diabetes mellitus. *J Clin Endocrinol Metab*. 2010;95(11):5045–5055.
35. Yu EW, Putman MS, Derrico N, Abrishamanian-Garcia G, Finkelstein JS, Bouxsein ML. Defects in cortical microarchitecture among African-American women with type 2 diabetes. *Osteoporos Int*. 2015;26(2):673–679.

36. Hein GE. Glycation endproducts in osteoporosis--is there a pathophysiologic importance? *Clin Chim Acta*. 2006;371(1-2):32–36.
37. Davis HM, et al. Short-term pharmacologic RAGE inhibition differentially affects bone and skeletal muscle in middle-aged mice. *Bone*. 2019;124:89–102.
38. Plotkin LI, Essex AL, Davis HM. RAGE signaling in skeletal biology. *Curr Osteoporos Rep*. 2019;17(1):16–25.
39. Suda T, Takahashi N, Udagawa N, Jimi E, Gillespie MT, Martin TJ. Modulation of osteoclast differentiation and function by the new members of the tumor necrosis factor receptor and ligand families. *Endocr Rev*. 1999;20(3):345–357.
40. Manavalan JS, et al. Circulating osteogenic precursor cells in type 2 diabetes mellitus. *J Clin Endocrinol Metab*. 2012;97(9):3240–3250.
41. Farr JN, Drake MT, Amin S, Melton LJ, McCready LK, Khosla S. In vivo assessment of bone quality in postmenopausal women with type 2 diabetes. *J Bone Miner Res*. 2014;29(4):787–795.
42. Yang J, Zhang X, Wang W, Liu J. Insulin stimulates osteoblast proliferation and differentiation through ERK and PI3K in MG-63 cells. *Cell Biochem Funct*. 2010;28(4):334–341.
43. Yamamoto M, Yamaguchi T, Yamauchi M, Yano S, Sugimoto T. Serum pentosidine levels are positively associated with the presence of vertebral fractures in postmenopausal women with type 2 diabetes. *J Clin Endocrinol Metab*. 2008;93(3):1013–1019.
44. Schwartz AV, et al. Pentosidine and increased fracture risk in older adults with type 2 diabetes. *J Clin Endocrinol Metab*. 2009;94(7):2380–2386.
45. Verzijl N, et al. Crosslinking by advanced glycation end products increases the stiffness of the collagen network in human articular cartilage: a possible mechanism through which age is a risk factor for osteoarthritis. *Arthritis Rheum*. 2002;46(1):114–123.
46. Vashishth D, Gibson GJ, Khoury JI, Schaffler MB, Kimura J, Fyhrie DP. Influence of nonenzymatic glycation on biomechanical properties of cortical bone. *Bone*. 2001;28(2):195–201.
47. Thomas CJ, Cleland TP, Sroga GE, Vashishth D. Accumulation of carboxymethyl-lysine (CML) in human cortical bone. *Bone*. 2018;110:128–133.
48. O'Grady KL et al. Development and validation of mass spectroscopy assays for Nε-(1-carboxymethyl)-L-lysine and pentosidine in renal failure and diabetes. *J Appl Lab Med*. 2020. In press.
49. Farr JN, Khosla S. Cellular senescence in bone. *Bone*. 2019;121:121–133.
50. Farr JN, Almeida M. The spectrum of fundamental basic science discoveries contributing to organismal aging. *J Bone Miner Res*. 2018;33(9):1568–1584.
51. Palmer AK, Tchkonia T, LeBrasseur NK, Chini EN, Xu M, Kirkland JL. Cellular senescence in type 2 diabetes: a therapeutic opportunity. *Diabetes*. 2015;64(7):2289–2298.
52. Rosen CJ, Bouxsein ML. Mechanisms of disease: is osteoporosis the obesity of bone? *Nat Clin Pract Rheumatol*. 2006;2(1):35–43.
53. Medrikova D, Jilkova ZM, Bardova K, Janovska P, Rossmeisl M, Kopecky J. Sex differences during the course of diet-induced obesity in mice: adipose tissue expandability and glycemic control. *Int J Obes (Lond)*. 2012;36(2):262–272.
54. Pettersson US, Waldén TB, Carlsson PO, Jansson L, Phillipson M. Female mice are protected against high-fat diet induced metabolic syndrome and increase the regulatory T cell population in adipose tissue. *PLoS One*. 2012;7(9):e46057.
55. Stubbins RE, Holcomb VB, Hong J, Núñez NP. Estrogen modulates abdominal adiposity and protects female mice from obesity and impaired glucose tolerance. *Eur J Nutr*. 2012;51(7):861–870.
56. Farr JN, et al. Independent roles of estrogen deficiency and cellular senescence in the pathogenesis of osteoporosis: evidence in young adult mice and older humans. *J Bone Miner Res*. 2019;34(8):1407–1418.
57. Rakshit K, Qian J, Gaonkar KS, Dhawan S, Colwell CS, Matveyenko AV. Postnatal ontogenesis of the islet circadian clock plays a contributory role in β-cell maturation process. *Diabetes*. 2018;67(5):911–922.